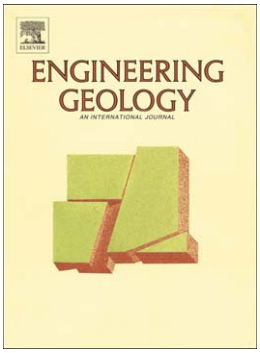

Investigation of the dynamic strain responses of sandstone using multichannel fiber-optic sensor arrays

Yankun Sun, Qi Li, Duoxing Yang, Chengkai Fan, An Sun

PII: S0013-7952(16)30248-4
DOI: doi: 10.1016/j.enggeo.2016.08.008
Reference: ENGEO 4363

To appear in: *Engineering Geology*

Received date: 15 April 2016
Revised date: 15 August 2016
Accepted date: 17 August 2016

Please cite this article as: Sun, Yankun, Li, Qi, Yang, Duoxing, Fan, Chengkai, Sun, An, Investigation of the dynamic strain responses of sandstone using multichannel fiber-optic sensor arrays, *Engineering Geology* (2016), doi: 10.1016/j.enggeo.2016.08.008

Investigation of the dynamic strain responses of sandstone using multichannel fiber-optic sensor arrays

Yankun Sun [a, b], Qi Li [a, *], Duoxing Yang [c], Chengkai Fan [a, b], An Sun [d]

[a] *State Key Laboratory of Geomechanics and Geotechnical Engineering, Institute of Rock and Soil Mechanics (IRSM), Chinese Academy of Sciences, Wuhan 430071, China*

[b] *University of Chinese Academy of Sciences, Beijing 100049, China*

[c] *Key Laboratory of Crustal Dynamics, Institute of Crustal Dynamics, China Earthquake Administration, Beijing 100085, China*

[d] *International Institute for Urban Systems Engineering, Southeast University, Nanjing 210096, China*

ABSTRACT:

In the process of rock mechanical experiments, strain-response measurement is a most fundamental and most essential procedure for geomechanical researchers. The main objective of this paper is to point out the feasibility and the superiority of the application of a novel multichannel fiber Bragg grating (FBG) sensor arrays for dynamic strain-response measurements of cylindrical specimen subjected to uniaxial compression. The principle, design, and embedment of multichannel FBG sensors used in the experiment are briefly described. To fully monitor the strain history of the sandstone cylinder in uniaxial compression, six circumferential FBG sensors, four lateral FBG sensors, linear variable differential transformers (LVDT) built-in machine have been utilized for spatially monitoring small radial and axial strains along the height of the specimen, respectively. The experimental results indicate that the proposed FBG sensors can successfully provide a full-field view of the surface strains, as well as detect the potential crack locations within the specimen, and strains measured by multichannel FBG sensors are in good agreement with the results of LVDT, especially in the axial strains. Hence, it could be inferred that multichannel FBG sensor arrays are capable of measuring dynamic strain responses of sandstone specimen in multistage compression, which would greatly strengthen experimental basis for further application and theoretic research of in-situ field monitoring.

*Keywords***:** Fiber Bragg grating (FBG); Multichannel sensor arrays; Uniaxial compression testing (UCT); Sandstone; Strain response; Damage

1. Introduction

Dynamic strain monitoring plays an essential role in mechanical characterization analysis of sub-and core-scale specimens**,** health assessment of industry-scale geotechnical structures, etc. One of the basic and most used methods of testing which is performed on rock samples is determination of uniaxial compressive strength and deformability (Kuhinek et al. 2011; Ranjith et al. 2004; Xie et al. 2011; Xu et al. 2013; Yu et al. 2016). Over the past several decades, there have been various instrumentations and implementations for strain measurement such as linear variable differential transformers (LVDTs) (Ibraim and Di Benedetto 2005; Yimsiri et al. 2005), electrical resistance strain gauge (ESG) (Kovačič et al. 2015; Montero et al. 2011; Motra et al. 2014; Raghuwanshi and Parey 2016; Ramos et al. 2015), digital image correlation (DIC) (Lin and Labuz 2013; Mehdikhani et al. 2016; Munoz et al. 2016; Walter 2011), digital terrestrial photogrammetry (DTP) (Firpo et al. 2011; Sturzenegger and Stead 2009) and extensometer (Feng et al. 2010; Jia et al. 2012; Perusek et al. 2001). Although it is generally agreed that these preexisting monitoring technologies can be comparatively accurate and reliable during the whole service life of the measurands respectively, intrinsic defects such as electromagnetic interference, signal loss, time-consumption and labor-intensity, uneasy acquisition, low resolution, and high cost remain intact, therefore they are deemed unsuitable for dynamic real-time and in-situ strain monitoring in field-scale engineering applications. Additionally, in terms of the sample heterogeneity and experimental complexity, it is important to note that these methods mentioned above can also barely implement high resolution and full-field simultaneous strain measurements with multiple sensors in harsh laboratory conditions (high temperatures, high pressures, corrosive acids, etc.).

Fiber Bragg grating (FBG) based sensing technology has been universally appreciated as the most promising candidate to effectively measure strain, temperature, pressure, vibration, ultrasound and other measurands (Sun et al. 2015). Owing to its outstanding advantages such as small size, flexibility, anti-corrosion, resistance to high pressures and high temperatures (HPHT), immunity to electromagnetic interference (EMI), large-scale multiplexing capability, wavelength-encoded characters, linearity, and so forth (Kou et al. 2012; Lai et al. 2013; Sun et al. 2013; Ye et al. 2014), it has a huge range of applications in aerospace (Davis et al. 2012), energy (Marques et

al. 2015; Shivananju et al. 2013), and maritime (Prasad et al. 2009; Razali et al. 2015), oil and gas downhole (Nellen et al. 2003; Schmidt-Hattenberger et al. 2004; Villnow et al. 2014; Zhou et al. 2012), biomedicine (Dziuda et al. 2013; Mishra et al. 2010; Roriz et al. 2013), acoustics (Silva et al. 2015; Takuma et al. 2014; Wu and Okabe 2014), and especially for structural health monitoring (SHM) in various civil infrastructures (Ecke and Schmitt 2013; Elshafey et al. 2016; Gage et al. 2014; Sanada et al. 2012; Torres et al. 2011; Weng et al. 2015; Xu et al. 2014; Zhu et al. 2015). However, it is worth noting that there are certain demerits of the FBG sensors. Because of more fragility of FBG sensor, some effective sensor package and protection methods are required. In addition, the FBG sensors and their interrogators are relatively expensive in comparison with conventional systems. And if high measurement resolution can be approached, FBG sensors are quasi-distributed fiber-optic monitoring technology and less powerful for the measurement of average strain or displacement than distributed optical sensors, such as Brillioun optical time domain analysis (BOTDA) or Brillouin Optical Time Domain Reflectometry (BOTDA).

Through these comparisons mentioned above, it could be found that in virtue of mechanical/electrical deformation of in-built components of conventional strain sensors, applied strains are deduced indirectly, so the measured strains are to a great extent dependent on properties of sensor components. The conventional strain measurements, such as ESGSs and LVDTs tend to be less stable over long periods of time due to decay and hence are suitable for short-term monitoring only. In addition, they can be easily deteriorated by water. In addition to these drawbacks, their each sensing unit needs many cables and wires for handling, which will suffer from electro-magnetic interference and electrical noise and it would further contaminate the measured strains. As for the conventional extensometer, it entails manual recording of data, which could be tedious, and for another, it will be obstructed by various installations in the in-situ applications. Besides, for the digital monitoring methods, the main limitation is that the devices frequently demand physical movement and could put the monitored structure out of service during the testing period (Yang et al. 2007). However, FBGs is an optical sensor made of thin fiber of glass and silica to transmit light signals, and external mechanical strain is calculated by the shifts of the reflected signals in the fiber (Yang et al. 2007). Therefore, it is tempting to conclude that the

outstanding advantages make FBG stain sensors high-accuracy (one microstrain) to monitor permanently deep and ultra-deep subsurface environments.

Based on above-mentioned capabilities, it is concluded that FBG sensor can potentially serve as a viable alternative to ESG or LVDTs for real-time strain monitoring of core specimens in laboratory testing. To date, however, there are only a certain number of articles involved preliminarily in this field where FBG sensors have been tentatively bonded/embedded into core specimens for dynamic strain, crack propagation, and damage detections (Elshafey et al. 2016). Alvaro et al. (Castro-Caicedo et al. 2013) presented a packaging and calibration procedure for surface mounting of FBG sensors to measure longitudinal and transversal strains as occurs in gabbro specimens, as well as comparison and validation with ESG concurrently attached to the locations nearest the sensors. The final conclusion showed that response of FBG sensors was linear and reliable, the strain ranges in rocks were experimentally confirmed as a few tens of microstrain, and the influence of rock inhomogeneities could be diminished due to increased effective measurement area of the FBG sensor packaging. Chen et al. (Benjamin Smith 2014; Chen et al. 2014) conducted an initial experiment upon detecting the strain history of the cylindrical SCARC (simulated carbon ash retention cylinder) samples and fracture locations within the cylinder. Lee et al (Lee et al. 2011) explored the development of a modified fiber optic sensored triaxial testing device coupled with a force transducer, linear displacement sensor, and a series of gauge/differential pressure transducers, as well as some soil tests carried out to practically evaluate and validate the effectiveness of the device based on the available test results by Xu et al. (Xu et al. 2014).

In the past several decades, in virtue of the nature characteristics of maximal complexity, many uncertainties and little visibility (Baldwin 2014; Kersey 2000), it has been a crucial and challenging project to break through for geoscientists and reservoir engineers that how to realize high-accuracy, elaborative and permanent in-situ monitoring for the dynamic processes of unconventional energy exploitation and geological disposals in the deep subsurface formations, especially with the rapid expansion of CO_2 capture, utilization and storage (CCUS) (Xue et al. 2014), geothermal exploration, underground gas construction, shale gas development, enhanced oil recovery (EOR) (Sun et al. 2016). For these reasons, it is therefore evident to point out that

FBG-based sensing technology will be aroused great interests and industrial demands in future due to its intrinsic superiority adapting for harsh environments (Braga 2014; Nakstad and Kringlebotn 2008). Undoubtedly, considerable efforts have been devoted to the field applications based FBG in the oil and gas industry (Hull et al. 2010; Koelman et al. 2012; Zhou et al. 2010). However, it has been realized that there are only few studies focusing on core-scale reservoir simulated experiments using FBG sensors (Bao et al. 2013), especially with explicit consideration of the dynamic strain responses of reservoir rocks.

In this paper, a new distributed monitoring method based on multichannel FBG sensor arrays is proposed and implemented to measure the axial and radial strain variations along the surface of cylindrical core specimen subjected to multistage uniaxial loads which has not been reported till date to the best of our knowledge. Ten FBG sensors (written in five arrays) and two built-in LVDTs are installed to characterize the full-field strain profiles and predict the potential micro/macrocrack propagation. By comparing the results from the multichannel FBG sensor arrays with built-in LVDTs, the applicability and workability of this idea and setup are confirmed.

2. Principle and methodology of multichannel FBG sensors

2.1. Operating principle of the FBG sensing technology

Traditionally, single mode fiber-optic (SMF) is made up of core and cladding as well as the core with a refractive index slightly higher than the cladding due to the presence of some dopants. An FBG consists of a short segment of SMF with periodic modulation in refractive index of the fiber core along the axis of the fiber, and is generally treated as a wavelength specific deflector or filter. When broadband light source (BLS) is launched into the FBG, each reflected light peak is centered on the called Bragg wavelength and light of other wavelengths without significant attenuation is transmitted, as shown in Fig. 1. The reflected wavelength of an FBG can be expresses as (A.W. Morey and Melte 1989):

$$\lambda_B = 2n_{\text{eff}}\,\Lambda \tag{1}$$

where λ_B is the Bragg wavelength, n_{eff} is the effective refractive index of the grating in the fiber core and Λ is the grating interval.

INSERT FIGURE 1 HERE

In practice, n_{eff} and Λ are both directly influenced by changes in strain and ambient temperature. When the grating is subjected to an axial strain to FBG orientation and/or an occurrence of temperature gradient closest to FBG, n_{eff} and Λ must be linearly modified through the thermo-optic and strain-optic effects, respectively. Hence, the relative Bragg wavelength shift $\Delta\lambda_B$ due to strain and temperature changes of the single fiber can be written as (Othonos and Kalli 1999):

$$\Delta\lambda_B = 2\left(\Lambda\frac{dn_{\text{eff}}}{d\varepsilon} + n_{\text{eff}}\frac{d\Lambda}{d\varepsilon}\right)\varepsilon + 2\left(\Lambda\frac{dn_{\text{eff}}}{dT} + n_{\text{eff}}\frac{d\Lambda}{dT}\right)\Delta T$$

$$= \lambda_B(1-p_e)\varepsilon + \lambda_B(\alpha+\xi)\Delta T = S_\varepsilon\varepsilon + S_T\Delta T \quad (2)$$

where ε is the longitudinal strain on the FBG, ΔT is the temperature variation, p_e is the effective photo-optic constant of the optical fiber core material; α is thermal coefficient for the fiber, and the quantity ξ denotes the thermo-optic coefficient of the grating. Moreover, the strain and temperature coefficients of relative Bragg wavelength shifts are 0.78×10^{-6} $\mu\varepsilon^{-1}$ and 6.67×10^{-6} $^{\circ}\text{C}^{-1}$. For a silica-based FBG with central wavelength λ_B =1550 nm, the typical strain and temperature sensitivity are S_ε ≈1.21 pm/με and S_T ≈10.3 pm/℃.

Throughout the compression experiment, the thermal variation around the gratings is ignored, because the tests conducted in current study are completed in a relatively short time and room temperature in laboratory is deemed to remain constant. As for a temperature-free FBG, the Bragg wavelength shift is only dependent on the applied strain, described by:

$$\Delta\lambda_B/\lambda_0 = (1-p_e)\varepsilon = S_\varepsilon\varepsilon \approx 0.78\varepsilon \quad (3)$$

where the $\Delta\lambda_B$ is wavelength difference compared to the original Bragg wavelength, λ_0 , the p_e is an effective strain-optic constant defined as

$$p_e = \frac{n_{\text{eff}}^2}{2}[p_{12} - \upsilon(p_{11}+p_{22})] \approx 0.22\,\mu\varepsilon^{-1} \quad (4)$$

p_{11} and p_{12} are components of the strain-optic tensor, and υ is Poisson's ratio. As illustrated Eqs. (3) and (4), when strain on an FBG sensor varies, it is known that the relative Bragg wavelength shift approximately equals to 0.78 multiplying by strain value (i.e., linear behavior), and then the applied strain can be calculated neglecting thermal effect and additional environmental fluctuations. Hence, for measurement of strain, the essence of FBG based sensing is to accurately identify $\Delta\lambda_B$.

To sum up, through the analysis of these principles, it is very clear that measurement of Bragg wavelength opens out primly dynamic change processes of real-time small strain in an FBG.

2.2. Design and embedment of multichannel FBG sensors

Fig. 2 shows the detailed design components of multichannel FBG sensors in one array used this experiment. In order to minimize losses/attenuations due to bending or transmission, the transmission medium throughout the optical path employs standard single-mode fibers (i.e., SMF-28e Corning®), which is ITU-T Recommendation G.652.D-compliant. Multichannel FBG sensors with two or four individual FBG in one array were fabricated. These sensing gratings were coupled with different Bragg wavelengths along a single fiber over long distances, which will enable the FBG interrogator to record all the sensors simultaneously using wavelength division multiplexing (WDM) scheme, which can record data at a rate of 200 Hz with a typical resolution of 1 με.

INSERT FIGURE 2 HERE

The gratings were placed at equal distance in 35 mm length fiber. This helps to locate the position of the sensors in sandstone core after installation. The optional wavelengths have been allocated in the range of 1538 nm-1561 nm to avoid overlapping in the optical spectrum and ensure that each sensor operates within a unique spectral range (usual 3-5 nm interval) in an array, whose technical specifications are detailed in Table 1. The length of the grating elements of 10 sensors was 10 mm. The FBG sensors were recoated with epoxy resin AB glue whose curing cycle is 2h at 80℃, to improve the mechanical strength and coupling stiffness of the FBG sensors embedded into sandstone core. Eventually, an integral system of multichannel FBG sensors array is fabricated and used in this study, as illustrated in Fig. 3.

INSERT FIGURE 3 HERE

In order to sensor the spatial distribution of the strain profile along the height of the specimen, three radial FBG arrays and two axial FBG arrays, an array consisting of two or four rows with a SMF carrying one FBG sensor, are bonded to the core.

Besides, it is also necessary to note that surface preparation becomes an extremely important task before bonding the fiber with FBG sensors on a non-uniform/rough surface of the sample, to avoid possible measurement errors induced by strain transfer. A sand and abrasive paper is used to furnish the area of FBG sensor installation. After furnishing, the surface of the specimen is cleaned by cotton immersed in methanol to facilitate the active bonding between the fiber and the surface of the specimen.

The sensors are installed in a sandstone core specimen using AB adhesive cured at room temperature in the required location. Fig. 4 presents schematic diagram of layout and embedment process of multichannel FBG sensors with cylindrical sandstone specimen. According to the process, three radial FBG arrays are installed firstly, and then two axial FBG arrays are embedded into the core with AB adhesive, whereas it is worth noting that radial sensors and axial sensors must not cross together against mutual interference. The radial and axial sensors are located with a longitudinal separation of 40 mm and 30 mm between them in one array, respectively.

Normally, before embedment of FBG sensors, evenly glue little AB adhesive for 2 h to improve the bonding strength of sandstone particles around the fixation sites, put FBG on them, and glue again as well as let stand for 24 h.

INSERT FIGURE 4 HERE

3. Experimental setup

3.1. Specimen preparation

A highly inhomogeneous sandstone rock core used in the experiment is obtained from rocks outcropping in the Sichuan Basin, Southwestern China. The specimen is shaped into a right circular cylinder that had a diameter of 50 mm and its aspect ratio (i.e. length to diameter ratio) maintained at 2.5 (seen Fig. 9 in section 4). The end faces and sides of the specimen are prepared

smooth and straight satisfying the recommendations by the International Society for Rock Mechanics (ISRM) standard, and by the end of the experiment, the specimen always keep dry state. Table 2 lists the main properties of sandstone core. Although some inevitable machining tolerances occurred because of processing imperfections, the tolerance could be neglected in view of its unapparent alteration of the final testing results (Feng et al. 2015).

3.2. Test apparatus

The core specimen is subjected to a static or dynamic axial loading under different rates by a digital controlled electro-hydraulic servo testing machine (i.e. RMT-150C Servohydraulic System developed by Institute of Rock and Soil Mechanics, Chinese Academy of Sciences in Wuhan, China), which has a maximum axial loading capacity of 1000 kN. The digital control system is fully digital and it is capable and flexible to operate loading rate under either axial-force rate control or axial-displacement rate control feedback signal using an in-built computer system, which makes arbitrary interference in the process of experiment to become a reality. Meanwhile, Owing to computer control system, it is of great convenience to handle automatically loading, unloading as well as going back to the initial state.

Additionally, the rock specimen placed onto the bottom cap is instrumented by two LVDTs with measuring range of 2.5 mm orientated in the radial direction to measure the average radial strain ε_r and one travel sensor with measuring range of 50 mm mounted in the top cap to record the axial strain ε_a. In consideration of making better comparison with FBG sensors and LVDTs readings, the two LVDT probes are positioned the location adjacent to the grating R3 and R4, respectively. However, it is important to note here that the calculated axial strains captured by travel sensor are even bigger than the true strains of the specimen, because travel sensor is applied to measure the accumulated deformation from the bottom cap to the bottom of the load cell.

In this experiment, the applied axial load is controlled in a way keeping axial-load rate constant of 0.50kN/s. Axial load (by a load cell), axial strain (by one travel sensor) and radial strain (by two LVDT probes) values are acquired continuously by a multifunctional digital-controlled system (i.e., one PC). The dynamic strain-response of the sample in compression by ten FBG sensors are recorded simultaneously using an FBG interrogator designed for demodulating reflected signal and transferring treated signal to PC for software reprocessing and graphical display. Fig. 5 shows

the experimental setup including two parts, the electrohydraulic servo testing system and FBG sensing system.

INSERT FIGURE 5 HERE

3.3. Experimental Procedure

To better conduct this experiment, it is a crucial step that the cylindrical specimen with properly attached FBG sensors needs 24 hours' standing to completely cure AB adhesive, reinforce the mechanical strength of grating region, as well as impose a certain degree of prestrain, which will be part of FBG firmly coupled with the core. Moreover, owing to the fragility of SMF, high sensitivity of FBG sensor and small-sized core, minimize the impact on the curing FBG prior to the test.

Embedded with five arrays comprised of 10 FBG sensors in two optical channels, in this way, allow to obtaining distributed strain measurements, the sample is laid onto the baseplate of RMT-150C machine to test. The sensor locations are depicted in Fig. 4. Channel 1 is for the top ring with grating R1 and R2, Channel 2 is the middle ring with grating R3 and R4, Channel 3 recorded the bottom ring with grating R5 and R6; and channel 4 acquired the two axial ring with sensors A1-A4.

Traditionally, in this kind of experiments, the axial load is linearly increased, until reach the uniaxial compression strength (UCS) of the core and subsequently, the sample is unloaded. However, for this test, it is necessary to perform the loading process at a very low speed in order to allow the FBG real-time measurements (with higher frequency sampling, the FBG interrogator needs to gather mass data for pauses). In consequence, some stops are performed during the loading process in case the FBG measurements at high speeds may automatically exit. The procedure consisted in loading linearly until reaching the desired load level and, at this level, make a stop for measuring.

In this study, the testing machine has been employed for loading the core under uniaxial compression in force-controlled mode at a rate of 0.50 kN/s up to failure. The loading process are involved in three periods: preloading, multistage loading (a pattern of several stop intervals during

loading) and unloading. The whole workflow of the testing machine during compression can be appreciated in Fig. 6. In the preloading stage, the axial force of 1 kN is default for RMT-150C machine. Whereafter, the loads are applied, which range from 2 kN to 34 kN with different increments of 1 kN, 2 kN or 3 kN, with a loading stop took less than 2 min between two adjacent loading stages.

The schematic diagram of three main stages of the uniaxial compression test and corresponding FBG sensors responses recorded are appreciated in Fig. 7. The bare fiber with ten FBG sensors in five arrays are epoxied to the cylinder surface (spatial locations depicted in Fig. 7**a**), and these sensors serve as both strain monitoring along the axis of the fiber core and localized crack detectors. During initial sandstone specimen compression, the cylinder will undergo significant tension and the occurrence of microcracks (Fig. 7**b**), and then after the peak stress takes place, progressive and generalized fractures in the rock surface are likely to interconnected rupture (Fig. 7**c**).

To better obtain and explain the information of the strain profile and history of the testing sample, it is crucial to have a good knowledge of the reflected signal of FBG sensors during compression. For this reason, the response relations between the wavelength variations and trends of FBG sensors and the strain or/and stress of the core in different loading stages are analyzed before the test.

Fig. 7**d** demonstrates the spectrum graphs of axial sensor A1 (in red) and radial sensor R1 (in cyan) in three stages. In the course of the experiment, the sensor A1 will be subjected to developing compression with the spectrum shifting to low wavelength, which is also validated as negative $\Delta\lambda_B$. But on the contrary, the sensor R1 is restrained by external tension as its spectra drifting high wavelength ($+\Delta\lambda_B$). Furthermore, the gradient of $\Delta\lambda_B$ of sensors A1 and R1 is progressively small due to compaction with time, and the decreasing degree of the former is greater than the latter because of the axial load only. Apparently, it can be easily pointed out that those points are also deduced from the curves as is appreciated by Fig. 7**e**.

INSERT FIGURE 6 HERE

INSERT FIGURE 7 HERE

4. Results and discussion

In this section, the results for the experiment performed with the sandstone core placed on servo testing machine and using the multichannel FBG sensor arrays and built-in LVDT measurements technologies are introduced.

The ten FBG sensors in four channels, simultaneously controlled by an FBG interrogator connected with four FC/APC, should be operated ahead of time to demodulate the wavelengths before preloading and to determine if all sensors hardware and software operate as expected. Continuous monitoring of the wavelength shifts are performed in a nearly constant room temperature environment throughout the experimental process to avoid perturbations induced by temperature changes. The radial and axial strain history recorded by FBGs and LVDTs is presensted in Fig. 8 and marked in different colors.

INSERT FIGURE 8 HERE

As indicated in Fig. 8, it is quite apparent to find that there is a similar ladder-type change trends of the strain responses of six FBG sensors in the axial and radial directions under different compression stages and intervals, especially for the situation of the two/foursensors belonging to the same array. In accordance with the loading processes (see in Fig. 6), the actual results are also in good agreement with the strain readings of the FBGs and LVDTs in the same measuring range.

In Fig. 8**a**, the localized radial strain profiles of the specimen are characterized distributed by the sensors R1 to R6 from the first 500 s. Specially noted that strains recorded by sensors R1 and R2 of channel 1 possess a relatively stable deviation between them within the first 331s and are close to the measured values of the LVDT probes, which can be fully inferred that the top of the sample remains relatively intact (crack initiation) and LVDT probes are closest to the two gratings. But subsequently, the strain of sensor R2 occurs abnormal bounce at 331.5s, manifesting that the potential large crack near the grating R2 is forming first. In the three radial sensor arrays, the strain data from the top array (including R1 and R2) indicate that the adjacent domain to the sensor has been in tensioned state, which varies almost simultaneously with the loading mode before 330 s; the strain output from the middle array comprising sensors R3 and R4 shows no big

jump in the compression process, especially slow convergence together, and this has fully demonstrated that the middle area near sensors deforms evenly and have insignificant rock homogeneity of rock; For the bottom array incorporating gratings R5 and R6, the strains appear big changes, so this shows that the specimen has been subjected to compressive status transitioning to tension and local microcracks propagates gradually. These conclusions are in a good agreement with the investigations from Benjamin Smith et al. (Smith et al. 2013), in which has pointed out that every functioning sensor reported a period of significant tensile strain increase followed by a reaction to fracture.

In addition, for the sake of realizing the initial strain state of the sensors, the preliminary stage of loading is magnified between 148s and 160s. Obviously, sensors R1, R2 and R3 are subjected to tensioned (positive strain) while grating R4, R5, and R6 are compressed (negative strain) due to without applying prestress during sensors installation or microcrack shrinkage. In the face of this state, a proper correction is required before strain calculation, such as right glue lectotype (Uchida et al. 2015).

Normally, uniaxial compression has a great influence on the axial strain revealed in Fig. 9. The strain history recorded by the four sensors (A1-A4) of the channel 4, as depicted in Fig. 8**b**, is significant variation owing to the dominance of the axial loading. From 145 s to 175 s, the sensors are tensioned strongly, corresponding strain ranging 250 με to 650 με. In the first several stages, sensors A2 and A3 show that the strain gradient is reversed (circled in yellow), implying that the specimen is mainly in elastic state. Furthermore, the strain of sensor A4 reduces to zero for an instant and the state lasts until the end. These indicate that sensor A4, the end sensor of the channel 4, has been broken and thus a macrocrack emerges. Unlike the sensor A4, the strain reduces to zero and instantaneously increases to a certain positive strain occurred in the sensor A1, which states clearly that grating A1 has experienced an instantaneous convert from compression to tension, but has not yet been destroyed. Based on the strain reactions in Fig. 8b, it can be speculated that surface peeling has achieved full penetration near the top sensor A1 and immediately propagated to the bottom region (A1) at 320 seconds due to the specimen coring from the weathered sandstone outcrop and its interface direction of crack propagation is from the top surface (across A1 grating region) extending to the diagonal (near to A4 sensor) of the specimen,

which is more clearly marked in red shown in Fig. 9**b**. For another thing, the global axial strain measured by LVDT already exceeded 1200 με at around 300 s, thus LVDT is not a significant indicator of localized strain reactions and concurrent microcracks in adjacent regions.

During the experiment, there are two significant damage occurred: one is the thin-bedded surface peeling with a soft crepitation (red line in Fig. 9b, c) and the other is rock failure with a loud crepitation and rapid unloading until the end (white line in Fig. 9c), which are mutually validated the inferences and correspondingly shown in Figs. 8 and 9, respectively. Hence, the multichannel FBG sensor arrays can correctly measure the dynamic strain responses and potential crack locations of the specimen in temporal and spatial distribution. More importantly, these reliable and high-precision data of rock deformation are extremely useful and valuable to provide the accumulations of raw data and theoretical mechanism reserves for further experimental analysis, numerical simulation and field applications. While there exist certain difficulties and gaps that this monitoring system is applied to real field applications, it is a first step to conduct a meaningful attempt in elaborate laboratory experimental investigation into rock geomechanics based on FBG technology, as well as is crucial and necessary basis to establish for more complex experiments and in-situ monitoring applications.

INSERT FIGURE 9 HERE

5. Conclusions

High-precision monitoring of dynamic strain response is a vitally meaningful and challenging task for researchers. In view of the above-mentioned advantages of FBG sensing technology, the paper presents a novel multichannel FBG sensors array for on-specimen strain measurement in a conventional uniaxial compression experiment.

The concept is based on aligning FBG array sensors, along a bare fiber, which are bonded to the specimen surface in the axial and radial directions. The strain-responses are simultaneously measured by the FBG arrays and in-built LVDTs and the test results are presented and interpreted in detail, which provide a new insight into the determination of dynamic strain response and the

characterization of full-field strain profile. The main findings obtained from this investigation are as follows.

(1) The effectiveness of the multichannel FBG sensors array to monitor the dynamic strain responses of sandstone core specimen subjected to uniaxial compression with high accuracy and resolution is validated. Although there exists certain error fluctuation between two FBG sensors belonging to the same array, the interaction effects are insignificant because they are written into the respective fiber and glued separately. Thus, each grating can independently function to collect date effectively and sufficiently employed the proposed methods in the study.

(2) According to the results from FBG sensors, it turns out that that there is a smilar ladder-type response trend of the strains under different loading stages and stops. The responses of axially embedded FBG sensors are larger than those radially embedded. Besides, it is proved that the strain trend coincides with the processes of the loading history.

(3) The multichannel FBG sensors array can successfully capture the real-time information of the full-field strain history, help predict the localized microcrack propagation within the core, determine the location of the potential macrocrack emergence. These conclusions can be verified by two significant damage that are thin-bedded surface peeling and rock failure, which are clearly characterized by the system in the experiment.

(4) Built-in LVDTs from the mechanical testing machine can be utilized to further validate the accuracy of above-mentioned inferences. The results recorded by LVDTs in the test are found to be in good agreement with those from the FBG sensors. However, the results also show that there are greater deviations originated from the axial LVDTs to the axial FBG sensors than those from the radial sensors, respectively.

It should be noted that the work reported in this paper is an effort and trial on the strain response of sandstone core specimen under uniaxial compression neglecting the influence of temperature. Further investigation may move onto the improvement of encapsulation, the effect of temperature on FBG and laboratory experiments on other sedimentary rock cores in more complex conditions.

Acknowledgements

This work is financially supported by the National Natural Science Foundation of China (grant nos. 41274111, 51308109) and the Natural Science Foundation of Jiangsu (grant no. BK20130620). We would like to gratefully acknowledge the financial support of the National Department Public Benefit Research Foundation of MLR, China (grant no. 201211063-4-1) and the Hundred Talent Program of the Chinese Academy of Sciences (grant no. O931061C01). The authors also wish to thank FANG Da (SEU), LIU Xuehao (IRSM) and ZHANG Hua (IRSM) for their experimental assistance or valuable suggestions. Additionally, the authors give special thanks to the anonymous reviewers for their insightful comments on the manuscript of this article.

References

A.W. Morey, G. & Melte, W.G. 1989. Fibre Optic Gratings Sensors. *Fiber Optic and Laser Sensors VII*. SPIE.

Baldwin, C. 2014. Optical fiber sensing in the oil and gas industry: overcoming challenges. 9157C9154-9157C9154-9154.

Bao, B., Melo, L., Davies, B., Fadaei, H., Sinton, D. & Wild, P. 2013. Detecting Supercritical CO_2 in Brine at Sequestration Pressure with an Optical Fiber Sensor. Environmental Science & Technology, **47**, 306-313, doi: 10.1021/es303596a.

Benjamin Smith, S.E.C., Bin Shi, Guangqing Wei, and Zhengfu Bian. 2014. Pathologic Interpretation of Loading and Cracking Process of SCARC Specimens Using Fiber Bragg Gratings. *Characterization, Modeling, and Evaluation of Geotechnical Engineering Systems*, 1-8.

Braga, A. 2014. Optical Fiber Sensors for the Oil and Gas Industry. *Advanced Photonics*. Optical Society of America, Barcelona, BM3D.1.

Castro-Caicedo, A., Torres, P. & Lain, R. 2013. Packaging and testing of fiber Bragg gratings for use as strain sensor in rock specimens. *In*: Costa, M. (ed.) *8th Iberoamerican Optics Meeting and 11th Latin American Meeting on Optics, Lasers, and Applications*. SPIE, Bellingham.

Chen, S.-e., Smith, B. & Wang, P. 2014. Fiber Optics Sensing of Stressing and Fracture in Cylindrical Structures. *In*: Allemang, R., De Clerck, J., Niezrecki, C. & Wicks, A. (eds.) *Topics in Modal Analysis, Volume 7*. Springer New York, 287-293.

Davis, C., Tejedor, S., Grabovac, I., Kopczyk, J. & Nuyens, T. 2012. High-strain fiber bragg gratings for structural fatigue testing of military aircraft. Photonic Sensors, **2**, 215-224, doi: 10.1007/s13320-012-0066-3.

Dziuda, L., Krej, M. & Skibniewski, F.W. 2013. Fiber Bragg Grating Strain Sensor Incorporated to Monitor Patient Vital Signs During MRI. Ieee Sensors Journal, **13**, 4986-4991, doi: 10.1109/jsen.2013.2279160.

Ecke, W. & Schmitt, M.W. 2013. Fiber Bragg Gratings in Industrial Sensing. *Optical Fiber Communication Conference/National Fiber Optic Engineers Conference 2013*. Optical Society of America, Anaheim, California, OM3G.1.

Elshafey, A., Marzouk, H., Gu, X., Haddara, M. & Morsy, R. 2016. Use of fiber Bragg grating array and random decrement for damage detection in steel beam. Engineering Structures, **106**, 348-354, doi: 10.1016/j.engstruct.2015.10.046.

Feng, B., Xu, M.L., Zhao, T.F., Zhang, Z.J. & Lu, T.J. 2010. Triaxial extensometer for volumetric strain measurement in a hydrocompression loading test for foam materials. Measurement Science and Technology, **21**, 11, doi: 10.1088/0957-0233/21/11/115705.

Feng, X., Zhang, N., Zheng, X. & Pan, D. 2015. Strength Restoration of Cracked Sandstone and Coal under a Uniaxial Compression Test and Correlated Damage Source Location Based on Acoustic Emissions. PloS one, **10**, e0145757, doi: 10.1371/journal.pone.0145757.

Firpo, G., Salvini, R., Francioni, M. & Ranjith, P.G. 2011. Use of Digital Terrestrial Photogrammetry in rocky slope stability analysis by Distinct Elements Numerical Methods. International Journal of Rock Mechanics and Mining Sciences, **48**, 1045-1054, doi: 10.1016/j.ijrmms.2011.07.007.

Gage, J.R., Wang, H.F., Fratta, D. & Turner, A.L. 2014. In situ measurements of rock mass deformability using fiber Bragg grating strain gauges. International Journal of Rock Mechanics and Mining Sciences, **71**, 350-361, doi: http://dx.doi.org/10.1016/j.ijrmms.2014.07.021.

Hull, J.W., Gosselin, L. & Borzel, K. 2010. Well-Integrity Monitoring and Analysis Using Distributed Fiber-Optic Acoustic Sensors. *2010 IADC/SPE Drilling Conference and Exhibition*. Society of Petroleum Engineers, New Orleans, Louisiana, USA.

Ibraim, E. & Di Benedetto, H. 2005. New local system of measurement of axial strains for triaxial apparatus using LVDT. Geotechnical Testing Journal, **28**, 436-444, doi: 10.1520/gtj11630.

Jia, J.H., Hu, X.Y., Wang, N. & Tu, S.T. 2012. Test verification of an extensometer for deformation measurement of high temperature straight pipes. Measurement, **45**, 1933-1936, doi: 10.1016/j.measurement.2012.03.037.

Kersey, A.D. 2000. Optical fiber sensors for permanent downwell monitoring applications in the oil and gas industry. Ieice Transactions on Electronics, **E83C**, 400-404.

Koelman, J.V.V., Lopez, J.L. & Potters, H. 2012. Optical Fibers: The Neurons For Future Intelligent Wells. *SPE Intelligent Energy International*. Society of Petroleum Engineers, Utrecht, The Netherlands.

Kou, J.-L., Ding, M., Feng, J., Lu, Y.-Q., Xu, F. & Brambilla, G. 2012. Microfiber-Based Bragg Gratings for Sensing Applications: A Review. Sensors, **12**, 8861-8876, doi: 10.3390/s120708861.

Kovačič, B., Kamnik, R., Štrukelj, A. & Vatin, N. 2015. Processing of Signals Produced by Strain Gauges in Testing Measurements of the Bridges. Procedia Engineering, **117**, 795-801, doi: http://dx.doi.org/10.1016/j.proeng.2015.08.249.

Kuhinek, D., Zoric, I. & Hrzenjak, P. 2011. Measurement Uncertainty in Testing of Uniaxial Compressive Strength and Deformability of Rock Samples. Measurement Science Review, **11**, 112-117, doi: 10.2478/v10048-011-0021-2.

Lai, M., Karalekas, D. & Botsis, J. 2013. On the Effects of the Lateral Strains on the Fiber Bragg Grating Response. Sensors, **13**, 2631-2644.

Lee, J.T., Tien, K.C., Ho, Y.T. & Huang, A.B. 2011. A Fiber Optic Sensored Triaxial Testing Device. Geotechnical Testing Journal, **34**, 103-111.

Lin, Q. & Labuz, J.F. 2013. Fracture of sandstone characterized by digital image correlation. International Journal of Rock Mechanics and Mining Sciences, **60**, 235-245, doi: 10.1016/j.ijrmms.2012.12.043.

Marques, R.D., Prado, A.R., Antunes, P.F.D., Andre, P.S.D., Ribeiro, M.R.N., Frizera-Neto, A. & Pontes, M.J. 2015. Corrosion Resistant FBG-Based Quasi-Distributed Sensor for Crude Oil Tank Dynamic Temperature Profile Monitoring. Sensors, **15**, 30693-30703, doi: 10.3390/s151229811.

Mehdikhani, M., Aravand, M., Sabuncuoglu, B., Callens, M.G., Lomov, S.V. & Gorbatikh, L. 2016. Full-field strain measurements at the micro-scale in fiber-reinforced composites using digital image correlation. Composite Structures, **140**, 192-201, doi: 10.1016/j.compstruct.2015.12.020.

Mishra, V., Singh, N., Rai, D.V., Tiwari, U., Poddar, G.C., Jain, S.C., Mondal, S.K. & Kapur, P. 2010. Fiber Bragg grating sensor for monitoring bone decalcification. Orthopaedics & Traumatology: Surgery & Research, **96**, 646-651, doi: http://dx.doi.org/10.1016/j.otsr.2010.04.010.

Montero, W., Farag, R., Diaz, V., Ramirez, M. & Boada, B.L. 2011. Uncertainties associated with strain-measuring systems using resistance strain gauges. Journal of Strain Analysis for Engineering Design, **46**, 1-13, doi: 10.1243/03093247jsa661.

Motra, H.B., Hildebrand, J. & Dimmig-Osburg, A. 2014. Assessment of strain measurement techniques to characterise mechanical properties of structural steel. Engineering Science and Technology, an International Journal, **17**, 260-269, doi: http://dx.doi.org/10.1016/j.jestch.2014.07.006.

Munoz, H., Taheri, A. & Chanda, E.K. 2016. Pre-Peak and Post-Peak Rock Strain Characteristics During Uniaxial Compression by 3D Digital Image Correlation. Rock Mechanics and Rock Engineering, 1-14, doi: 10.1007/s00603-016-0935-y.

Nakstad, H. & Kringlebotn, J.T. 2008. Oil and gas applications: Probing oil fields. Nat Photon, **2**, 147-149.

Nellen, P.M., Mauron, P., Frank, A., Sennhauser, U., Bohnert, K., Pequignot, P., Bodor, P. & Brandle, H. 2003. Reliability of fiber Bragg grating based sensors for downhole applications. Sensors and Actuators a-Physical, **103**, 364-376, doi: 10.1016/s0924-4247(02)00430-2.

Othonos, A. & Kalli, K. 1999. Fiber Bragg Gratings: Fundamentals and Applications in Telecommunications and Sensing. Artech House, London.

Perusek, G.P., Davis, B.L., Courtney, A.C. & D'Andrea, S.E. 2001. An extensometer for global measurement of bone strain suitable for use in vivo in humans. Journal of Biomechanics, **34**, 385-391, doi: http://dx.doi.org/10.1016/S0021-9290(00)00197-4.

Prasad, G., Asokan, S., Tatavarti, R. & Ieee. 2009. Detection of Tsunami Wave Generation and Propagation Using Fiber Bragg Grating Sensors. Ieee, New York.

Raghuwanshi, N.K. & Parey, A. 2016. Experimental measurement of gear mesh stiffness of cracked spur gear by strain gauge technique. Measurement, **86**, 266-275, doi: http://dx.doi.org/10.1016/j.measurement.2016.03.001.

Ramos, T., Braga, D.F.O., Eslami, S., Tavares, P.J. & Moreira, P.M.G.P. 2015. Comparison Between Finite Element Method Simulation, Digital Image Correlation and Strain Gauges Measurements in a 3-

Point Bending Flexural Test. Procedia Engineering, **114**, 232-239, doi: http://dx.doi.org/10.1016/j.proeng.2015.08.063.

Ranjith, P.G., Fourar, M., Pong, S.F., Chian, W. & Haque, A. 2004. Characterisation of fractured rocks under uniaxial loading states. International Journal of Rock Mechanics and Mining Sciences, **41**, 361-361, doi: 10.1016/j.ijrmms.2003.12.067.

Razali, N.F., Abu Bakar, M.H., Tamchek, N., Yaacob, M.H., Latif, A.A., Zakaria, K. & Mandi, M.A. 2015. Fiber Bragg grating for pressure monitoring of full composite lightweight epoxy sleeve strengthening system for submarine pipeline. Journal of Natural Gas Science and Engineering, **26**, 135-141, doi: 10.1016/j.jngse.2015.06.020.

Roriz, P., Frazao, O., Lobo-Ribeiro, A.B., Santos, J.L. & Simoes, J.A. 2013. Review of fiber-optic pressure sensors for biomedical and biomechanical applications. Journal of Biomedical Optics, **18**, 18, doi: 10.1117/1.jbo.18.5.050903.

Sanada, H., Sugita, Y. & Kashiwai, Y. 2012. Development of a multi-interval displacement sensor using Fiber Bragg Grating technology. International Journal of Rock Mechanics and Mining Sciences, **54**, 27-36, doi: 10.1016/j.ijrmms.2012.05.020.

Schmidt-Hattenberger, C., Otto, P., Toepfer, M., Borm, G. & Baumann, I. 2004. Development of fiber Bragg grating (FBG) permanent sensor technology for borehole applications. 124-127.

Shivananju, B.N., Kiran, M., Nithin, S.P., Vidya, M.J., Hegde, G.M. & Asokan, S. 2013. Real time monitoring of petroleum leakage detection using etched fiber Bragg grating. *International Conference on Optics in Precision Engineering and Nanotechnology (Icopen2013)*. SPIE, Singapore, Singapore 5.

Silva, R.E., Tiess, T., Becker, M., Eschrich, T., Rothhardt, M., Jager, M., Pohl, A.A.P. & Bartelt, H. 2015. All-fiber 10 MHz acousto-optic modulator of a fiber Bragg grating at 1060 nm wavelength. Optics Express, **23**, 25972-25978, doi: 10.1364/oe.23.025972.

Smith, B., Chen, S.E., Shi, B., Wei, G.Q. & Bian, Z.F. 2013. Fiber optic monitoring of SCARC specimens with crack location prediction. *In*: Yu, T.Y., Gyekenyesi, A.L., Shull, P.J., Diaz, A.A. & Wu, H.F. (eds.) *Nondestructive Characterization for Composite Materials, Aerospace Engineering, Civil Infrastructure, and Homeland Security 2013*. Spie-Int Soc Optical Engineering, Bellingham.

Sturzenegger, M. & Stead, D. 2009. Close-range terrestrial digital photogrammetry and terrestrial laser scanning for discontinuity characterization on rock cuts. Engineering Geology, **106**, 163-182, doi: 10.1016/j.enggeo.2009.03.004.

Sun, A., Wu, Z. & Huang, H. 2013. Power-compensated displacement sensing based on single mode-multimode fiber Bragg grating structure. Optics Communications, **311**, 140-143, doi: http://dx.doi.org/10.1016/j.optcom.2013.08.033.

Sun, Y., Li, Q., Li, X., & Yang, D. 2015. Progress of real-time monitoring technology in oil and gas industry based on Fiber Bragg Grating sensing. Science & Technology Review, **33**, 84-91. doi: 10.3981/j.issn.1000-7857.2015.13.014

Sun, Y., Li, Q., Yang, D. & Liu, X. 2016. Laboratory core flooding experimental systems for CO_2 geosequestration: An updated review over the past decade. Journal of Rock Mechanics and Geotechnical Engineering, **8**, 113-126, doi: 10.1016/j.jrmge.2015.12.001.

Takuma, M., Hisada, S., Saitoh, K., Takahashi, Y., Kobayashi, Y., Kadono, A., Murata, A., Iwata, S. & Sasaki, T. 2014. Acoustic Emission Measurement by Fiber Bragg Grating Glued to Cylindrical Sensor Holder. Advances in Materials Science and Engineering, 12, doi: 10.1155/2014/274071.

Torres, B., Payá-Zaforteza, I., Calderón, P.A. & Adam, J.M. 2011. Analysis of the strain transfer in a new FBG sensor for Structural Health Monitoring. Engineering Structures, **33**, 539-548, doi: 10.1016/j.engstruct.2010.11.012.

Uchida, S., Levenberg, E. & Klar, A. 2015. On-specimen strain measurement with fiber optic distributed sensing. Measurement, **60**, 104-113, doi: 10.1016/j.measurement.2014.09.054.

Villnow, M., Bosselmann, T., Willsch, M. & Kaiser, J. 2014. FBG system for temperature monitoring under electromagnetic immersed and harsh oil and gas reservoir environment. 915797-915797-915794.

Walter, T.R. 2011. Low cost volcano deformation monitoring: optical strain measurement and application to Mount St. Helens data. Geophysical Journal International, **186**, 699-705, doi: 10.1111/j.1365-246X.2011.05051.x.

Weng, X.L., Ma, H.H. & Wang, J. 2015. Stress Monitoring for Anchor Rods System in Subway Tunnel Using FBG Technology. Advances in Materials Science and Engineering, 7, doi: 10.1155/2015/480184.

Wu, Q. & Okabe, Y. 2014. Novel real-time acousto-ultrasonic sensors using two phase-shifted fiber Bragg gratings. Journal of Intelligent Material Systems and Structures, **25**, 640-646, doi: 10.1177/1045389x13483028.

Xie, H., Pei, J., Zuo, J. & Zhang, R. 2011. Investigation of mechanical properties of fractured marbles by uniaxial compression tests. Journal of Rock Mechanics and Geotechnical Engineering, **3**, 302-313, doi: http://dx.doi.org/10.3724/SP.J.1235.2011.00302.

Xu, D.S., Borana, L. & Yin, J.H. 2014. Measurement of small strain behavior of a local soil by fiber Bragg grating-based local displacement transducers. Acta Geotechnica, **9**, 935-943, doi: 10.1007/s11440-013-0267-y.

Xu, T., Ranjith, P.G., Wasantha, P.L.P., Zhao, J., Tang, C.A. & Zhu, W.C. 2013. Influence of the geometry of partially-spanning joints on mechanical properties of rock in uniaxial compression. Engineering Geology, **167**, 134-147, doi: 10.1016/j.enggeo.2013.10.011.

Xue, Z., Park, H., Kiyama, T., Hashimoto, T., Nishizawa, O. & Kogure, T. 2014. Effects of hydrostatic pressure on strain measurement with distributed optical fiber sensing system. Energy Procedia, **63**, 4003-4009, doi: http://dx.doi.org/10.1016/j.egypro.2014.11.430.

Yang, Y.W., Bhalla, S., Wang, C., Soh, C.K. & Zhao, J. 2007. Monitoring of rocks using smart sensors. Tunnelling and Underground Space Technology, **22**, 206-221, doi: http://dx.doi.org/10.1016/j.tust.2006.04.004.

Ye, X.W., Su, Y.H. & Han, J.P. 2014. Structural Health Monitoring of Civil Infrastructure Using Optical Fiber Sensing Technology: A Comprehensive Review. Scientific World Journal, **2014**, 1-11, doi: 10.1155/2014/652329.

Yimsiri, S., Soga, K. & Chandler, S.G. 2005. Cantilever-type local deformation transducer for local axial strain measurement in triaxial test. Geotechnical Testing Journal, **28**, 445-451, doi: 10.1520/gtj11432.

Yu, C., Ji, S. & Li, Q. 2016. Effects of porosity on seismic velocities, elastic moduli and Poisson's ratios of solid materials and rocks. Journal of Rock Mechanics and Geotechnical Engineering, **8**, 35-49, doi: http://dx.doi.org/10.1016/j.jrmge.2015.07.004.

Zhou, X.L., Li, L.Z. & Yu, Q.X. 2012. Fiber Bragg Grating-Based Quasi-Distributed Temperature Sensor for Down-Hole Monitoring. Sensor Letters, **10**, 1486-1490, doi: 10.1166/sl.2012.2486.

Zhou, Z., He, J.P., Huang, M.H., He, J., Ou, J.P. & Chen, G.D. 2010. Casing Pipe Damage Detection with Optical Fiber Sensors: a Case Study in Oil Well Constructions. Advances in Civil Engineering, **2010**, 1-9, doi: 10.1117/12.848727.

Zhu, H.H., Shi, B., Yan, J.F., Zhang, J. & Wang, J. 2015. Investigation of the evolutionary process of a reinforced model slope using a fiber-optic monitoring network. Engineering Geology, **186**, 34-43, doi: 10.1016/j.enggeo.2014.10.012.

Fig. 1. Sensing principle of a bare fiber Bragg grating (FBG).

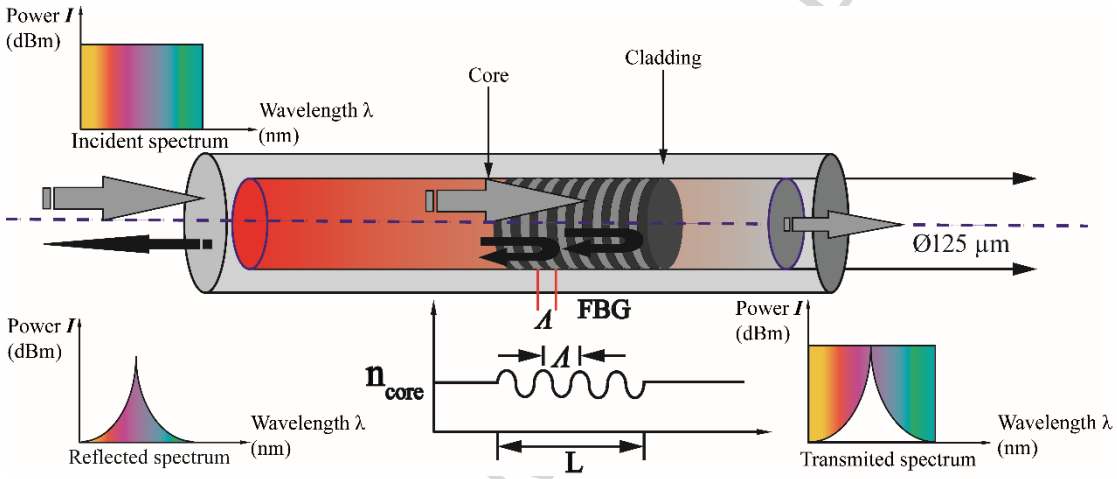

Fig. 2. Detailed design components of multichannel FBG sensors in one array.

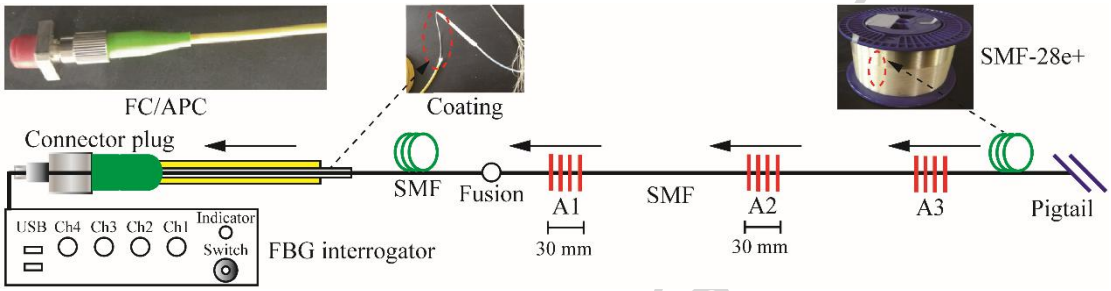

Fig. 3. A simplified schematic diagram of multichannel FBG sensors system.

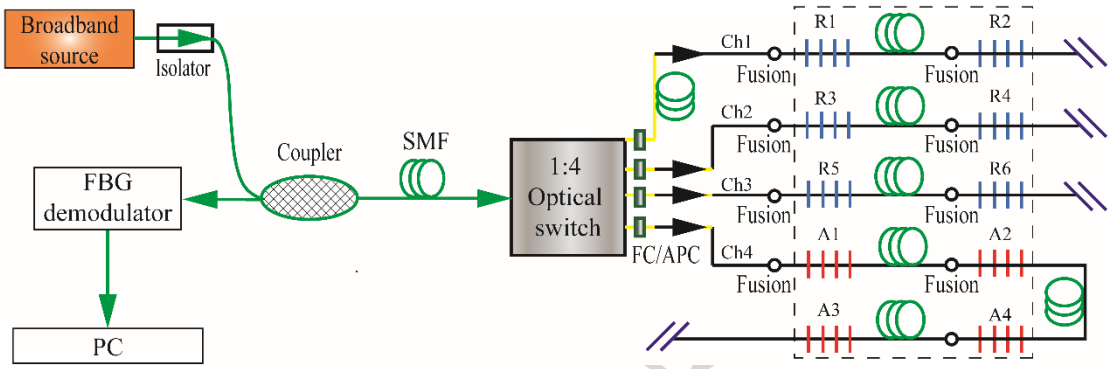

Fig. 4. Schematic diagram of layout and embedment process of multichannel FBG sensors pasted on sandstone specimen. (**a**)-(**c**) Radial layout of FBG sensors: (**a**) 3D radial FBG arrays, (**b**) top view of one FBG array and (c) its stretching view. (**d**)-(**e**) Axial layout of FBG sensors: (**d**) top view of 2 axial FBG arrays and (**e**) 3D axial FBG arrays. (**f**) 3D view of FBG sensors. (**g**) Developed view of FBG sensors.

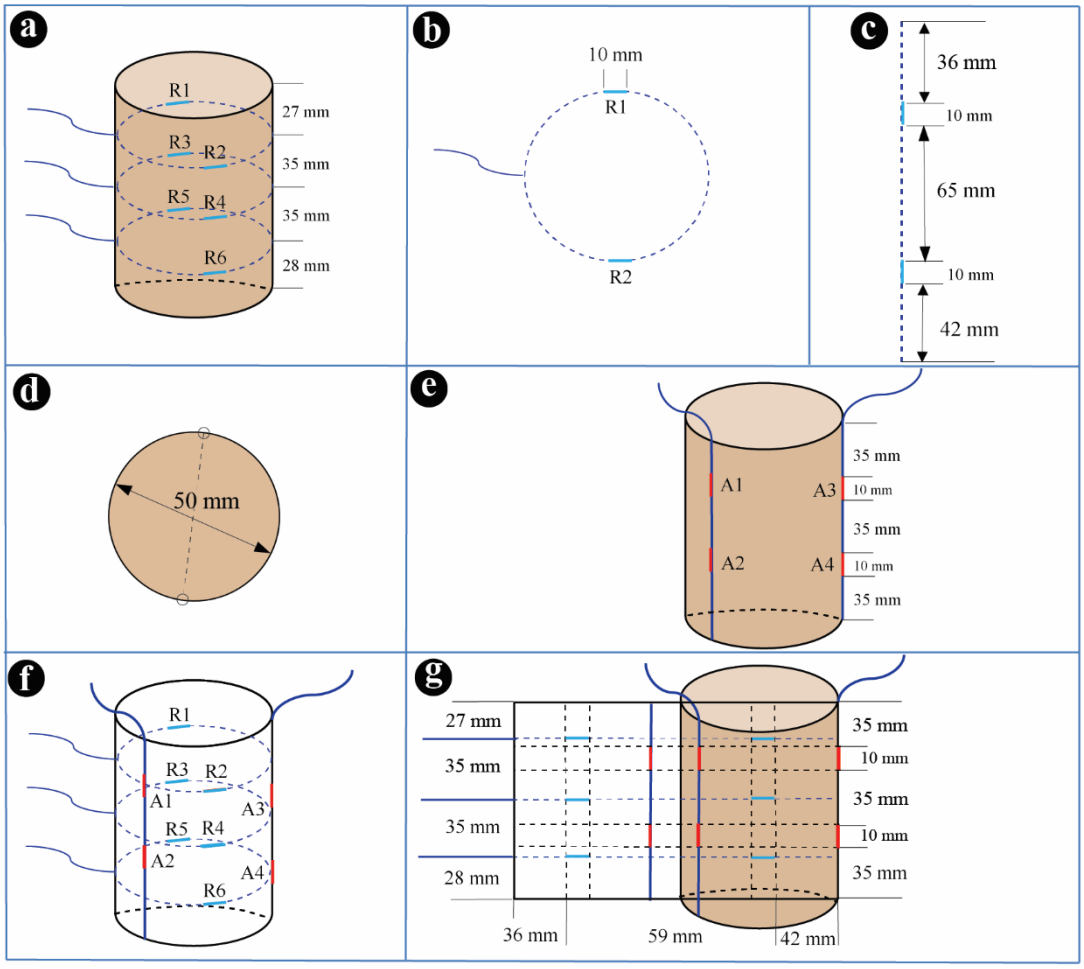

Fig. 5. Photographic view of experimental apparatus. (**a**) Digital controlled electro-hydraulic servo testing system and FBG interrogator during compression load. (**b**) Main structure segment of the loading device. (**c**) Detail view of the working platform of the testing machine.

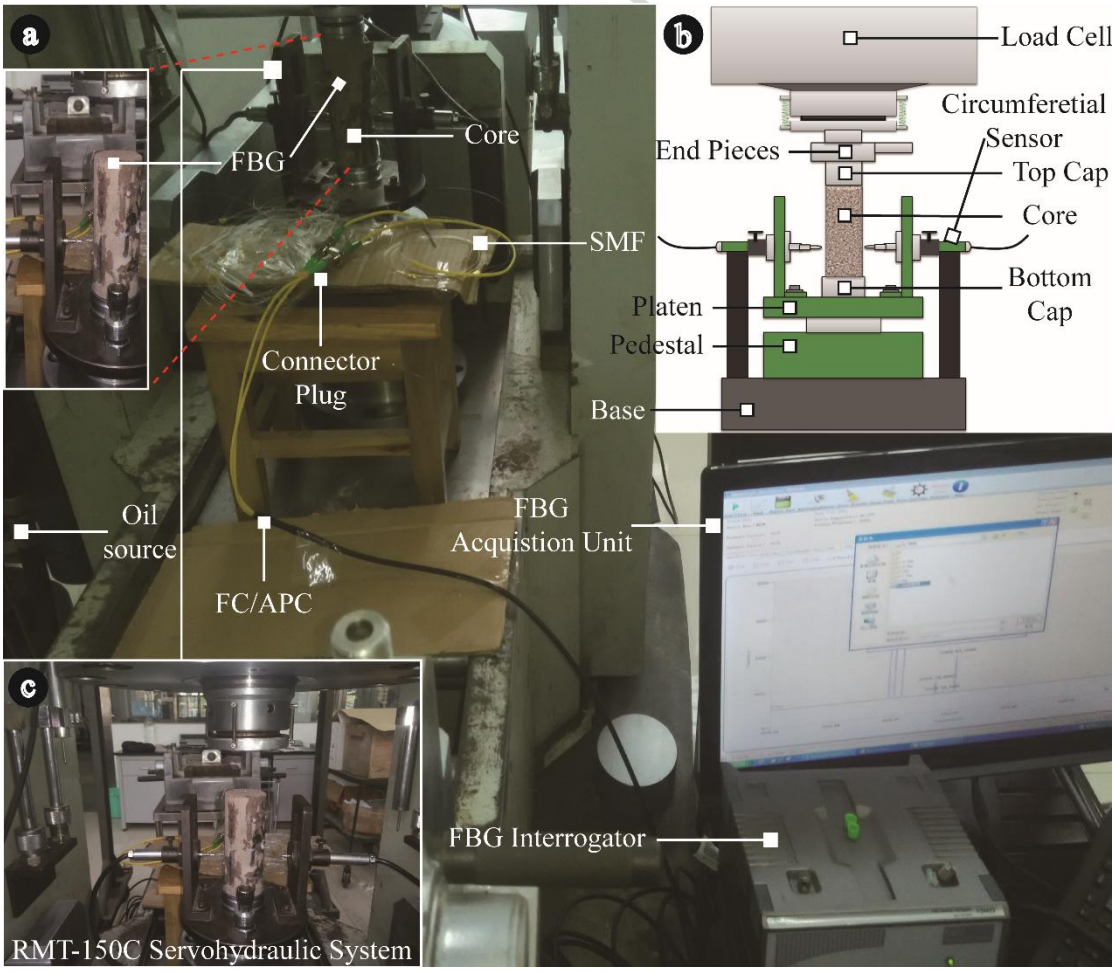

Fig. 6. The whole workflow of the testing machine during uniaxial compression.

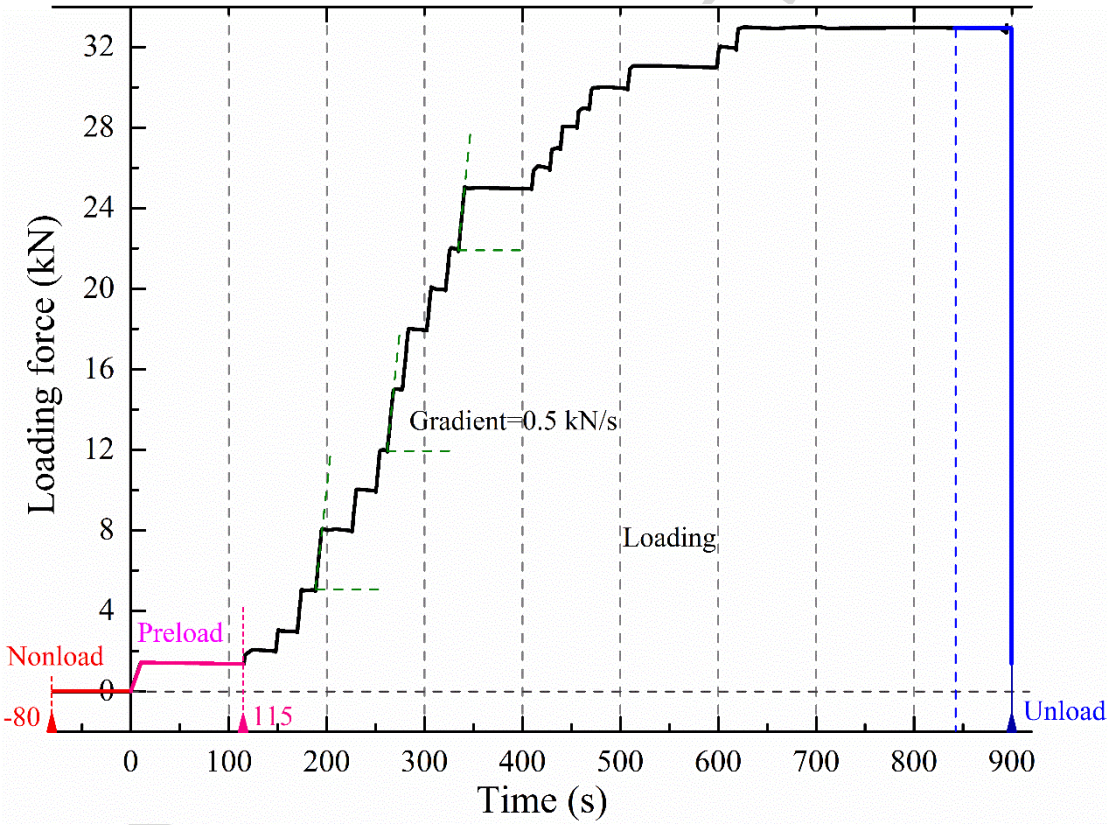

Fig. 7. The processes of schematic diagram of the uniaxial compression and FBG data manipulation. (**a**) Spatial locations of sensors in sandstone specimen. (**b**) The initial stage of loading process. (**c**) The peak stage of loading process. (**d**) Corresponding wavelength shifts of sensors A1 and R1: **I.** Nonloaded period, **II.** Loading period, and **III.** Max loading period. (**e**) Analogical results of ε_r or ε_a-t curves and ε_r or ε_a-λ_B curves.

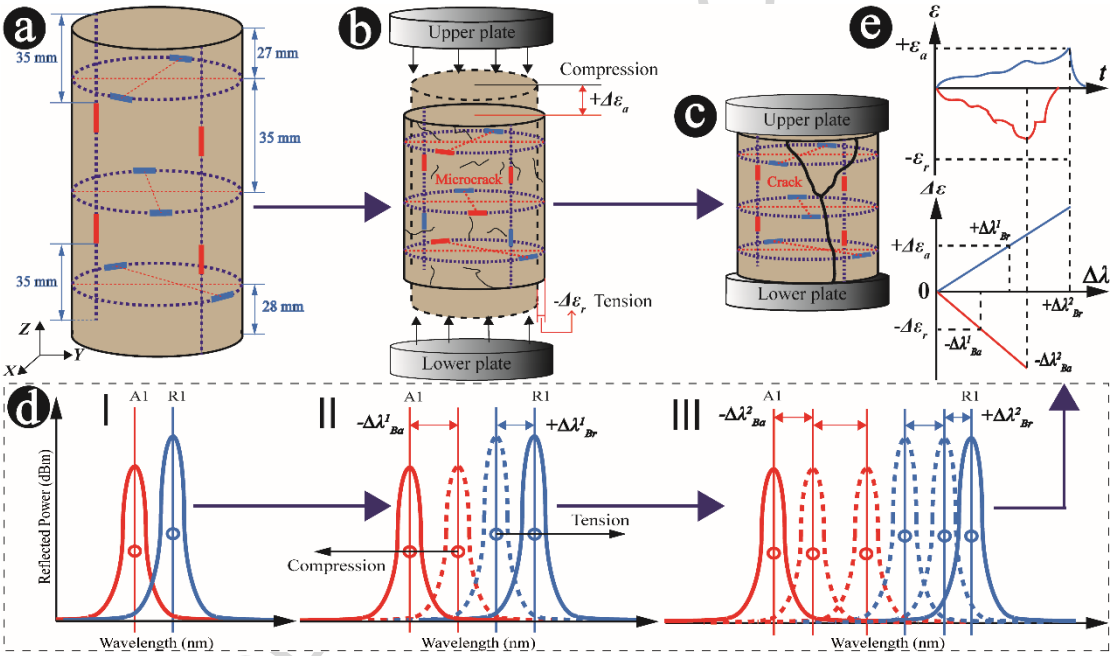

Fig. 8. Strain history of the sandstone specimen under stage compression using FBGs and LVDTs. (**a**) The radial strain-response recorded by six FBGs (two arrays) and two LVDT probes. (**b**) The axial strain-response recorded by four FBGs (one array) and one LVDT probe (in-built travel control).

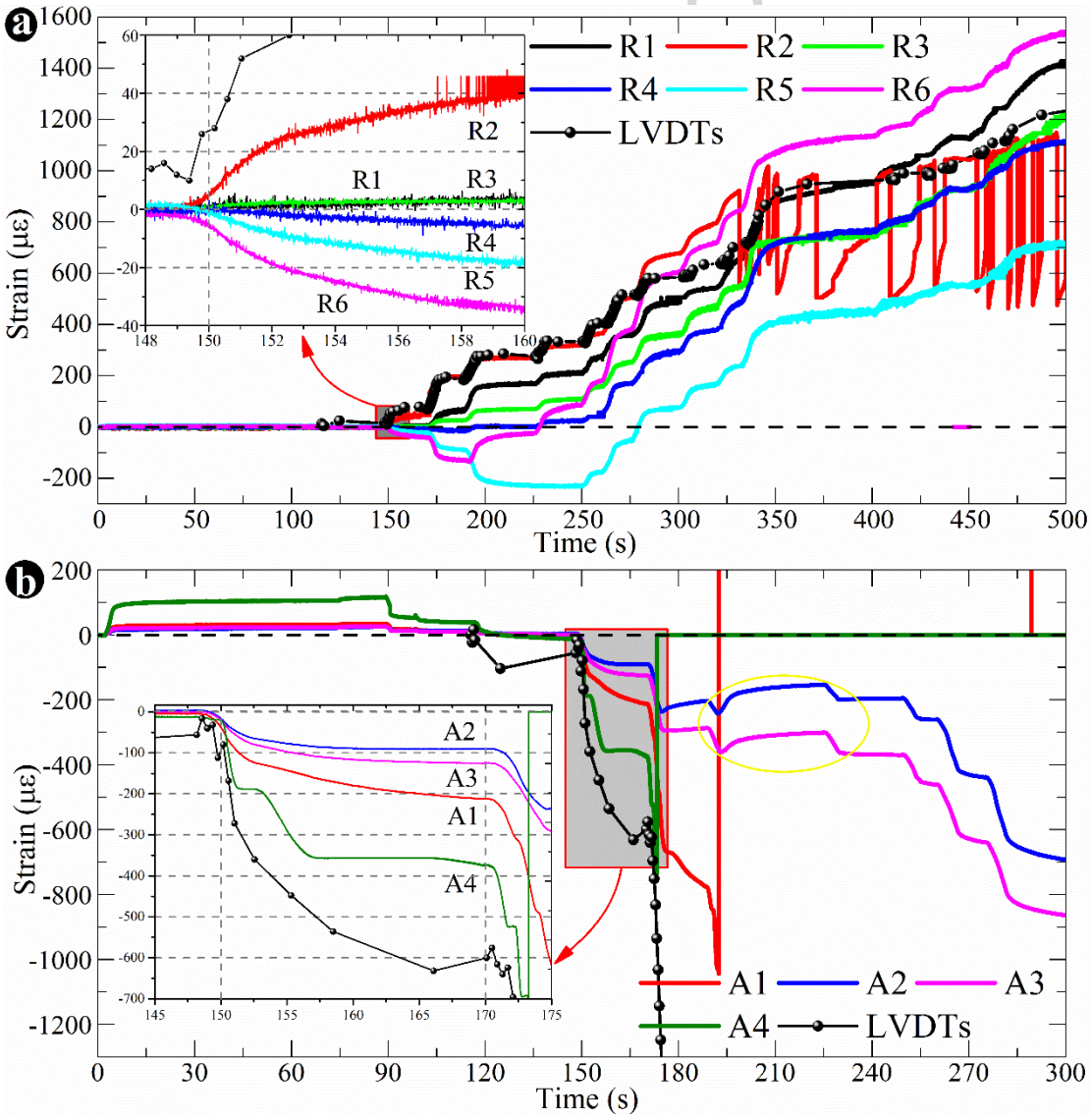

Fig. 9. Test results of sandstone specimen. (**a**) Stress-strain curves under uniaxial compression. (**b**) Surface peeling (in red dash lines) of the specimen at the initial loading stage. (**c**) The failure mode of the specimen (in white solid lines).

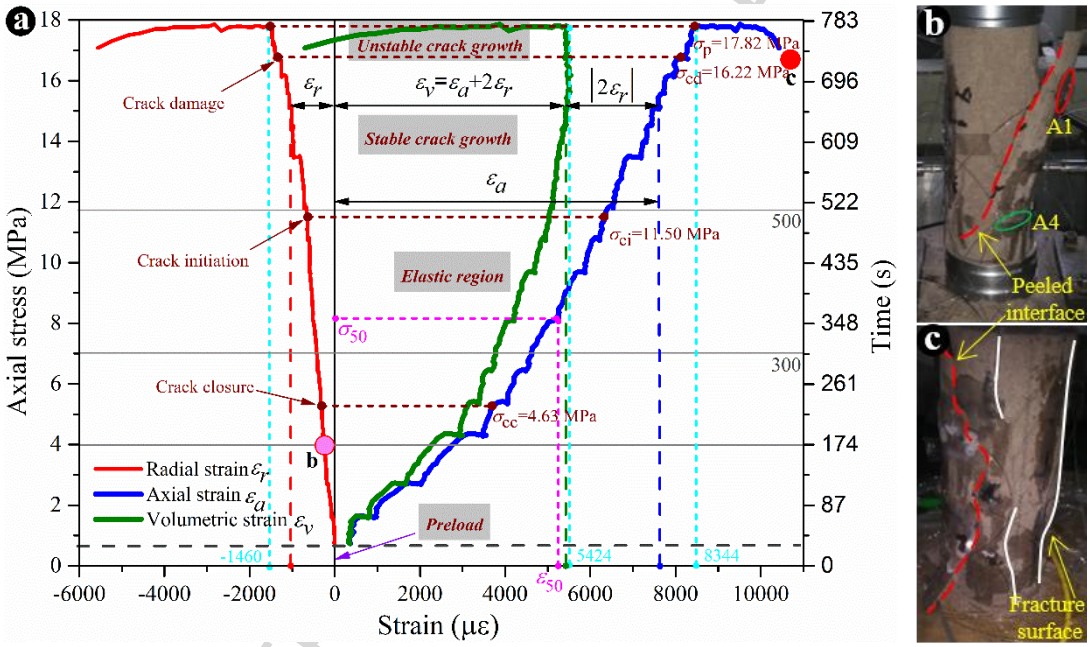

Table 1

Specifications of FBG applied to the test sample.

Component	R1	R2	R3	R4	R5	R6	A1	A2	A3	A4
$\boldsymbol{\lambda_B}$ (nm)	1538	1541	1544	1553	1556	1559	1547	1550	1553	1561
L (mm)	27.0	27.0	62.0	62.0	97.0	97.0	35.0	80.0	35.0	80.0
Channel	Ch1		Ch2		Ch3		Ch4			
Similarity	S_ε (pm/με)		Resolution (pm)		λ_B tolerance		Reflectivity	Recoating	FWHM	SMSR
	1.21±0.05		1.0		±0.3		0.5%-0.99%	Acrylate	0.1-0.5	>8 dB

L stands for the length from specimen top surface.

λ_B tolerance means the variable range of the central λ_B.

FWHM presents FBG width at 50% (-3 dB) from FBG maximum reflectivity, measured from reflection spectra.

SMSR indicates highest secondary peak larger than 3 dB amplitude within +/- 3 nm from λ_B.

Table 2

Physical and mechanical properties of the test sample.

Specimen	Diameter (mm)	Height (mm)	Cross-sectional area (mm^2)	Volume (mm^3)	Density ($kg \cdot m^{-3}$)
Sandstone	49.55	124.92	1928.29	240882.21	2431.25

Highlights

- A novel multichannel FBG sensor arrays was developed for sandstone specimen.
- FBG sensors conducted dynamic strain monitoring during multistage compression.
- The tests showed the strain profiles and potential crack locations in the specimen.
- The comparisons between FBG and LVDT confirmed the workability of our method.